HHS Public Access

Author manuscript

ACS Nano. Author manuscript; available in PMC 2018 January 24.

Published in final edited form as:

ACS Nano. 2017 January 24; 11(1): 797–805. doi:10.1021/acsnano.6b07196.

One-Component Supramolecular Filament Hydrogels as Theranostic Label-Free Magnetic Resonance Imaging Agents

Lye Lin Lock[†,‡,⬡], **Yuguo Li**[§,⬡], **Xinpei Mao**[‡], **Hanwei Chen**[§,‖], **Verena Staedtke**[⊥], **Renyuan Bai**[#], **Wang Ma**[†], **Ran Lin**[‡], **Yi Li**[‡], **Guanshu Liu**[*,§,¶], and **Honggang Cui**[*,†,‡,□,△]

[†]Department of Oncology, The First Affiliated Hospital of Zhengzhou University, 1 Jianshe Eastern Road, Zhengzhou 450052, Henan, China

[‡]Department of Chemical and Biomolecular Engineering and Institute for NanoBioTechnology, Johns Hopkins University, Baltimore, Maryland 21218, United States

[§]The Russell H. Morgan Department of Radiology and Radiological Science, Division of MR Research, Johns Hopkins School of Medicine, Baltimore, Maryland 21205, United States

[⊥]Department of Neurosurgery, Johns Hopkins School of Medicine, Baltimore, Maryland 21205, United States

[#]Department of Neurology, Johns Hopkins School of Medicine, Baltimore, Maryland 21205, United States

[□]Department of Oncology and Sidney Kimmel Comprehensive Cancer Center, Johns Hopkins School of Medicine, Baltimore, Maryland 21205, United States

[‖]Department of Radiology, Panyu Central Hospital, Guangzhou, China

[¶]F.M. Kirby Research Center for Functional Brain Imaging, Kennedy Krieger Institute, Baltimore, Maryland 21205, United States

[△]Center for Nanomedicine, The Wilmer Eye Institute, Johns Hopkins University School of Medicine, 400 North Broadway, Baltimore, Maryland 21231, United States

Abstract

Gadolinium (Gd)-based compounds and materials are the most commonly used magnetic resonance imaging (MRI) contrast agents in the clinic; however, safety concerns associated with

[*]**Corresponding Authors:** gliu10@jhmi.edu; hcui6@jhu.edu.

[⬡]**Author Contributions**

L. L. Lock and Y. Li contributed equally to the work.

Supporting Information

The Supporting Information is available free of charge on the ACS Publications website at DOI: 10.1021/acsnano.6b07196. Detailed methods (chemicals; synthesis and purification of molecules; mass and analytical characterization; PemFE isomer structure; and drug loading calculation) and some supporting results (TEM and cryo-TEM imaging, self-assembly of PemFE filaments and hydrogels, cytotoxicity assays and drug release experiments, and *in vitro* and *in vivo* CEST MRI study) (PDF)

ORCID

Guanshu Liu: 0000-0002-8188-4332

Honggang Cui: 0000-0002-4684-2655

Notes

The authors declare no competing financial interest.

their toxicities in the free ionic form have promoted the development of new generations of metal-free contrast agents. Here we report a supramolecular strategy to convert an FDA-approved anticancer drug, Pemetrexed (Pem), to a molecular hydrogelator with inherent chemical exchange saturation transfer (CEST) MRI signals. The rationally designed drug–peptide conjugate can spontaneously associate into filamentous assemblies under physiological conditions and consequently form theranostic supramolecular hydrogels for injectable delivery. We demonstrated that the local delivery and distribution of Pem–peptide nanofiber hydrogels can be directly assessed using CEST MRI in a mouse glioma model. Our work lays out the foundation for the development of drug-constructed theranostic supramolecular materials with an inherent CEST MRI signal that enables noninvasive monitoring of their *in vivo* distribution and drug release.

Graphical abstract

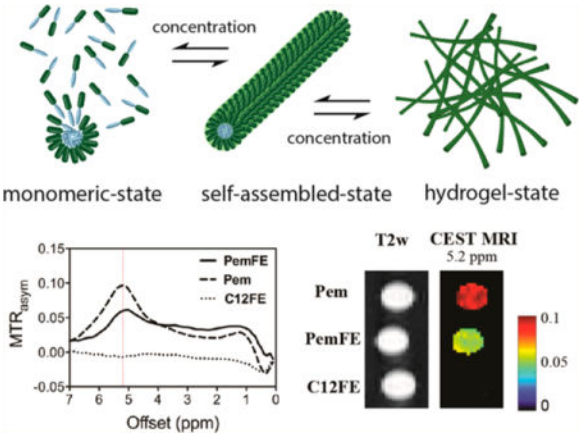

Keywords

molecular assembly; supramolecular nanofibers; MRI; CEST; anticancer drugs

Supramolecular nanostructures and hydrogels derived from small-molecule peptides and peptide conjugates are an emerging class of biomaterials that have received much attention initially in regenerative medicine and tissue engineering[1–7] and recently in drug delivery[8–21] and disease diagnosis.[22–24] In the context of drug delivery for cancer chemotherapy, the ability to monitor and track therapeutic agents is highly desirable to achieve a better disease prognosis and to comprehend treatment successes and failures.[25] To render real-time reporting of drug distribution upon *in vivo* administration, imaging-guided drug delivery or theranostic systems have been widely explored to incorporate chemo therapeutic drugs with different imaging modalities such as positron emission tomography (PET),[26] single-photon emission computed tomography (SPECT),[27,28] magnetic resonance imaging (MRI),[29,30] and ultrasonic[31] and fluorescence imaging.[32–35] Among them, MRI is one of the most commonly used diagnostic methods due to its superior spatial resolution and soft tissue contrast.[36] There have been several important attempts to incorporate an MRI modality into these peptide-based systems by introducing a metal chelator in the molecular design.[23,24,37–40] Although signal enhancement can be observed in these systems for the purpose of imaging, the potential toxicity of the chelated ions such as gadolinium (Gd) in the free form

at higher concentrations (*e.g.*, triggering nephrogenic systemic fibrosis[41] or deposition in the brain of patients[42]) undermines the intriguing properties of peptides and peptide conjugates as biocompatible materials.

Chemical exchange saturation transfer (CEST) is an emerging MRI contrast mechanism that utilizes a special MRI pulse sequence to selectively detect exchangeable protons at their unique chemical shift (frequency offset), thus translating them into frequency-specific molecular imaging agents.[43,44] The exchangeable protons are detected by the attenuation of the MRI (water) signal caused by the continuous transfer of the saturated (NMR signal being nulled) protons from the probes to their surrounding water molecules. Using the CEST approach, bio-organic molecules[45–48] containing exchangeable protons such as –O*H*, –N*H*, and –NH_2 groups can be saturated by a frequency-specific radiofrequency pulse. For example, a series of X-ray contrast agents, Iopamidol,[49] iopromide,[50,51] and iobitridol,[52] with an –NH proton were shown to exhibit a CEST MRI signal that enabled *in vivo* microenvironment pH mapping. More importantly, CEST can be potentially used to detect therapeutic drugs,[45,53,54] drug/gene delivery systems,[55,56] and their subsequent tumor responses in a “label-free” manner.[57–59] One unbeatable advantage of using CEST MRI for pursuing image-guided drug delivery is that, with the intrinsically endowed CEST contrast, extensive chemical labeling of bioactive molecules can be avoided, namely, “natural labeling”.

In this context, we report on the pioneering use of an FDA-approved anticancer drug, pemetrexed (Pem), as both a CEST MRI contrast agent and molecular building units to create theranostic supramolecular filament hydrogels. The use of therapeutic agents to create self-assembling drug amphiphiles represents an effective strategy to create one-component nanomedicines.[16,60–66] We chose the anticancer drug Pem because of its inherent CEST MRI signal at 5.2 ppm frequency offset from the resonance of water. By conjugation of pemetrexed with a rationally designed peptide, we show that the resultant conjugate can spontaneously form supramolecular filament hydrogels in aqueous solutions for injectable delivery into brain tumor sites, serving as both a therapeutic and diagnostic agent. Notably, the entire hydrogel system contains only water and the designed drug conjugate, thus affording a one-component label-free theranostic platform.

RESULTS AND DISCUSSION

Molecular Design

Pemetrexed is a chemotherapeutic drug (marketed under the trade name Alimta[67]) composed of aromatic amines and secondary amines in its chemical structure (Pem in blue, Figure 1a). These exchangeable protons possess a chemical shift of 9.9 ppm by NMR convention, or 5.2 ppm apart from water, and can be selectively saturated and transferred to bulk water through chemical exchange, resulting in a marked decrease of the water signal intensity (Figure 1b). Subsequently, the CEST contrast, the decrease in water signal intensity with and without saturation RF pulses, is quantified by the magnetization transfer ratio (MTR_{asym}), providing a way to quantify Pem using noninvasive MRI. In this case, Pem can be considered as a dual functional agent, both an anticancer drug and MRI contrast agent. Since Pem (Figure 1a) has a relatively low water solubility, conjugation of Pem with a short peptide of overall

hydrophilicity would result in an amphiphilic prodrug for potential formation of discrete nanostructures under physiological conditions (Figure 1c). To construct the Pem–peptide conjugate, we designed a short peptide sequence containing two glutamic acids and two phenylalanines to create a Pem drug amphiphile. Glutamic acid was chosen because it carries a negative charge on its side chain, which can minimize the cationic-induced cytotoxic effect commonly reported in positively charged nanoparticles.[68] The hydrophilic characteristic of glutamic acids (EE) is crucial to achieve the amphiphilic balance with the low-water-soluble Pem drug. Phenylalanine (FF) was incorporated to promote the self-assembly of PemFE (Figure 1a) through π–π interactions. The phenylalanine benzyl side chain has been shown to direct the self-assembly of amphiphilic peptide into nanotubes or nanofibers.[69–74] We found that the use of the two phenylalanine residues, instead of two valines or two glycines, greatly enhances the potential of our designed molecules to form supramolecular filamentous hydrogels. Details of the molecular synthesis and characterization can be found in the Supporting Information S1 (Figures S1–S3). The concept of self-assembling peptide–drug conjugates enables precise control of the high drug loading from the molecular design level.[64,65] In this particular construct, the Pem drug loading can be regarded as 100 wt % if considering the entire molecule as a prodrug, or 42 wt %, as defined by the ratio of the molecular mass of Pem to the total molecular weight of the PemFE conjugate (S1.5). In comparison, the conventional drug encapsulation method and the drug–polymer conjugation approach result in a typical drug loading of less than ~5 wt % and ~10 wt %, respectively.[75] The molecular masses of synthesized PemFE (MW = 979) and C12FE (MW = 774) molecules were confirmed using electrospray ionization mass spectroscopy (Figure S1), and their purity was confirmed using analytical HPLC (Figure S2). It should be noted that in our synthesis products, due to the presence of dual carboxylic acid functional sites, the target molecule PemFE coexists with its structural isomer, as denoted by an asterisk (*) in Figure 1a and Figure S3. We presume that their CEST properties are similar, given the long distance between the preserved aromatic amine and the conjugation sites. By replacing the Pem drug with a linear C12-hydrocarbon, the C12FE molecule was designed and synthesized as a control molecule, and its full chemical structure is shown in Figure S3c.

Molecular Self-Assembly and Characterization

The self-assembly of PemFE and C12FE was initiated by directly dissolving their respective lyophilized powder into Dulbecco's phosphate-buffered saline (1× DPBS). After aging over 24 h at room temperature, their self-assembled nanostructures were characterized using cryo-transmission electron microscopy (cryo-TEM) (S2). Cryo-TEM micrographs in Figure 2a,b show that both PemFE and C12FE self-assembled into filamentous nanostructures at a concentration of 4 and 10 mM, respectively. The corresponding diameters of PemFE and C12FE nanofibers are 9.1 ± 1.4 and 8.5 ± 0.9 nm measured from conventional TEM images (Figure S4), which are approximately twice the expected molecular length (~3.9 and ~3.2 nm, respectively). This suggests that these molecules are likely packed in a core–shell fashion within the observed filamentous assemblies.[5,76,77] According to the previous reports on peptide amphiphile assembly,[16,76,78] the observed one-dimensionality is likely a result of the hydrogel bonding among the FFEE peptide segments, working in concert with the aromatic interactions between phenylalanine side chains and between the aromatic portions

of the pemetrexed. The lengths of these filaments are typically in the range of several micrometers even at a concentration of 100 μM and increase when the conjugate concentration is increased; however, the exact evaluation of the filament length and length distribution cannot be achieved. At 30 mM, the assembly of both molecules led to the formation of self-supporting hydrogels in a 1× PBS solution, as shown in Figure 2c.

Given the therapeutic potential of the PemFE, we performed cytotoxicity assays to evaluate the potency of the Pem prodrug against the mouse glioma cell line, GL261, with free Pem and C12FE as control. Our results (Figure S5) suggested that the IC_{50} for PemFE is one order of magnitude higher than that of the free Pem (2.29 *vs* 0.13 μM). This compromised efficacy is expected and can be attributed to the retarded release of the free Pem from the prodrug as a result of the necessary degradation by enzymes of the peptidic auxiliary segment. Our results also suggested that the control peptide conjugate C12FE did not show any significant cell toxicity at concentrations up to 100 μM, implying the potential biocompatibility of the chosen peptide sequence.

Since the PemFE molecules are noncovalently linked within the supramolecular filaments, we expect an effective release of the conjugate from its hydrogels upon dilution/consumption through molecular dissociation. The release experiments were conducted on a PemFE hydrogel of 30 mM in a phosphate buffer at 37 °C, and samples were collected at a series of desired time points and stored at −30 °C. Upon completion of the sample collection, all the samples were measured using reverse-phase HPLC. The plot of cumulative release *versus* time (Figure S6) suggested a two-phase release mechanism: a relatively faster initial release followed by an almost linear release over the course of several days, with ~65% drug released within 8 days. Although the exact release profile may vary in a more complex *in vivo* setting, this study demonstrates clearly the potential of using Pem-bearing supramolecular filament hydrogels as a long-term therapeutic reservoir.

In Vitro CEST MRI Measurement

MRI measurements revealed that both Pem and PemFE filament hydrogels show a strong CEST signal at ~5.2 ppm at pH 7.4 and 37 °C (Figure 2). We first prepared PemFE, C12FE, and Pem at 10 mM concentration (in 1× PBS, pH 7.4, and 37 °C) and measured their respective CEST properties on a 9.4 T vertical bore Bruker MRI scanner using a previously reported procedure.[79] The CEST effect was displayed as Z-spectra (Figure 2d) and further quantified using MTR_{asym} (Figure 2e), as defined by $MTR_{asym} = (S^{-\Delta\omega} - S^{+\Delta\omega})/S_0$, where $S^{-\Delta\omega}$ and $S^{+\Delta\omega}$ are the MRI signal intensities after saturation at $-\Delta\omega$ and $+\Delta\omega$ frequency offsets from the water proton frequency (set at 0 ppm); S_0 is the intensity in the absence of a saturation pulse. Both Z-spectra and MTR_{asym} plots clearly showed a strong CEST signal at ~5.2 ppm. At this frequency offset, as shown in the color-coded CEST parametric map (Figure 2f), a marked CEST contrast can be appreciated between PemFE and the control molecule (C12FE). We therefore speculate this CEST signal arises from the aromatic primary amine's exchangeable proton on the Pem (~10 ppm using ^{1}H NMR spectrometry[80]). It is noteworthy that, as a result of the fast exchange rate, the CEST peak at 5.2 ppm is broadened and the exact offset to obtain the "peak" CEST effect was observed to be slightly shifted (ranging from 5.0 to 5.4 ppm) for samples measured at different solution pH or using

different saturation power (Figures S7). Our measurements also suggested that the CEST MRI signal (MTR_{asym} at 5.2 ppm) of both Pem and PemFE filaments increased linearly as their respective concentrations were increased from 100 μM to 10 mM (Figure S8).

We found that PemFE hydrogels typically showed lower CEST signals compared to free Pem (Figure 2e,f) at the same concentration. Part of this could be attributed to the fact that some of the aromatic amines of PemFE are embedded within the assemblies, limiting the accessibility of Pem-exchanging protons to the surrounding water. The suppression or acceleration of proton exchange rates, as a result of distinct water exposure of exchanging protons, has been studied to probe the differences in protein conformational structures.[81,82] Despite the suppressed effect observed here, the CEST signal of PemFE at 5.2 ppm offset is markedly higher compared to the control C12FE (Figure 2d–f), enabling direct MR imaging of Pem filament hydrogels, without the need for additional imaging contrast agents.

The apparent CEST effect is strongly dependent on the saturation parameters used to acquire CEST MRI images. Figure 3a shows that both Pem and PemFE (10 mM, pH 7.4) exhibited a linear increase with respect to higher saturation field strength (B_1). Considering a higher B_1 can also cause a severe direct water saturation effect and unwanted magnetization transfer effect for the *in vivo* cases, we chose B_1 = 3.6 μT for subsequent *in vivo* studies. Figure 3b shows the example of the QUEST (quantifying exchange rates using saturation time) analysis of saturation time (T_{sat})-dependent CEST effect of PemFE at pH 6 (dotted line), pH 7 (solid line), and pH 8 (dashed line). The same analysis was performed for Pem and C12FE, and the results are shown in Figure S9. As expected, MTR_{asym} at 5.2 ppm increases with increasing T_{sat} for Pem-containing molecules. However, for T_{sat} longer than 3 s, the CEST effect did not increase significantly. Therefore, a T_{sat} of 3 s was considered the optimal value and was used in the subsequent studies.

Interestingly, PemFE and C12FE exhibited different pH-dependence CEST contrast in the pH range from pH 6.0 to pH 8.5, as shown in Figure 3c. When pH is increased, both free Pem and PemFE have a biphasic response, *i.e.*, first increased and then decreased. The maximal CEST contrasts were observed at pH 7.4 and pH 7.0 for Pem and PemFE, respectively, while C12FE clearly showed a continuous decrease of CEST contrast when pH increases, although the maximal CEST contrast was only 0.01 ± 0.001. The correlation of Pem and PemFE CEST contrast to pH condition indicates that the exchange rate (k_{ex}) of the Pem amine proton changes dramatically at different pH values. To estimate the exchange rate (k_{ex}), we measured the MTR_{asym} values at 5.2 ppm with saturation time (T_{sat}) ranging from 0.5 to 6 s and analyzed the data using the previously reported QUEST method.[83] The pH dependence of the proton exchange rate (k_{ex}) of each compound is shown in Figure 3d. The estimated Pem proton exchange rate is on the order of 10^2–10^3 s^{-1}, which is comparable to k_{ex} reported in other literature.[48,52] Both Pem and PemFE clearly exhibited a biphasic k_{ex} function with respect to pH (Figure 3d). The initial pH-dependent increase is attributed to the gradual increase of exchange rate as the solution pH is increased in a way similar to all the base-catalyzed proton exchanges.[81] However, the second phase in which k_{ex} drops when pH further increases is unexpected. We speculate that the further increase of pH led to a k_{ex} value exceeding the slow-to-moderate exchange rate region (*i.e.*, $k_{ex} > \Delta\omega$), which instead compromises the CEST signal and results in a decrease of the apparent CEST contrast.

In Vivo CEST MRI Time-Point Study and Spatial Comparison

To assess the potential use of the PemFE hydrogel *in vivo*, a GL261 orthotopic brain tumor model was used. In brief, C57BL6 mice (female, 5–6 weeks, $n = 4$) were stereotactically injected with 2×10^4 GL261 cells in the right hemisphere of the brain. Twenty-five days after the inoculation of tumor cells, 10 μL of 30 mM PemFE hydrogel was injected into each tumor site using the same stereotactic settings. We chose a hydrogel concentration of 30 mM to investigate the feasibility of injecting the drug-containing hydrogels at the highest possible concentrations to obtain a steady release of a large dosage, while generating reasonable CEST signals and avoiding solubility issues. *In vivo* MRI was performed before and 2 and 96 h postinjection on a Biospec 11.7 T MRI scanner equipped with a 23 mm mouse brain volume coil. CEST MRI acquisition and data processing were performed as previously reported ($B_1 = 3.6$ μT and $T_{sat} = 3$ s).[79] As shown in Figure 4a, a localized but not uniform PemFE hydrogel distribution in the tumor could be observed by comparing the CEST MRI signal acquired at 2 h after the injection and that before injection. After 4 days, the PemFE hydrogel was still CEST detectable but appeared as a more uniform distribution over a larger area, indicating a slow gradient-driven diffusion to nearby tumor cells. Filament hydrogels are often regarded as injectable materials, but their network structures could be deformed to some extent under shear stress during the injection delivery process. Given the supramolecular and entanglement nature, the injected hydrogels are expected to recover to their original state after delivery.[13] Our study provides visual evidence of the distribution and recovery process of filament hydrogels in mouse glioma tumors using CEST MRI for up to 4 days postimplantation.

To further evaluate the imaging capability of the PemFE hydrogel, we quantitatively analyzed the CEST MRI signal at the injection site compared to its surrounding tumor regions. Figure 4b shows an overlay image of the CEST parametric map (threshold by $MTR_{asym} > -0.01$) at 2 h postinjection of the PemFE hydrogel and a T2w anatomical image. We chose two regions of interest (ROIs) in the tumor, with ROI1 representing the region having a strong CEST MRI signal elevation and ROI2 representing the region that has a low CEST MRI contrast. Then we repeated the same analysis on five mice. As shown in Figure 4c, the mean CEST contrast between the ROI1 (injection site in the tumor) and ROI2 (surrounding region in the corresponding tumor) was 0.024 in MTR_{asym}, which is statistically significant ($P = 0.045$, two-tailed, paired Student's *t*-test). This result indicates that CEST MRI is able not only to detect the location of the implanted hydrogel but also to assess the amount of drug qualitatively in the regions of interest.

CONCLUSION

In summary, we have developed an MRI-based theranostic filament hydrogel system that directly uses therapeutic agents as both the molecular building units and MRI contrast agents. With the inherent CEST MRI signal afforded by the anticancer drug pemetrexed at 5.2 ppm, the location, distribution, recovery, and drug release of the injected PemFE hydrogel could be monitored using CEST MRI in an orthotopic brain tumor mouse model. This MRI theranostic hydrogel platform also enables the possibilities for probing tumor recurrence. Furthermore, such an MRI approach no longer relies on the use of exogenous

MRI contrast agents such as gadolinium chelators. As recent studies have shown that the leakage and deposition of gadolinium ion can cause serious nephrogenic systemic fibrosis, our approach provides a safer way to accomplish image-guided drug delivery. While further therapeutic evaluations and molecular optimization are anticipated, the current study demonstrated a highly innovative strategy to construct metal-free MRI-guided drug delivery systems of high-potential supramolecular materials for clinical translation.

MATERIALS AND METHODS

Peptide Synthesis and Purification

The peptide Fmoc-FFEE was synthesized on a Focus XC automated peptide synthesizer (AAPPTEC, Louisville, KY, USA) with the scale of 0.25 mmol by using standard Fmoc-solid-phase synthesis techniques. Fmoc deprotection was followed using 20% 4-methylpiperidine in DMF solution for 15 min, repeating once. After Fmoc deprotection, lauric acid was manually coupled to the N-terminus of NH_2–FFEE with a lauric acid/HBTU/DIEA ratio of 4:4:6 relative to the peptide, shaking overnight at room temperature. The coupling of Pem was performed manually at the N-terminus of NH_2–FFEE with Pem/HBTU/DIEA at a ratio of 1.2:1.2:1.8 relative to the peptide, with shaking overnight at room temperature. In all cases, reactions were monitored by the ninhydrin test (Anaspec Inc., Fremont, CA, USA) for free amines. Both C12FE and PemFE were cleaved from the Wang resins using the standard cleavage solution of TFA/TIS/H_2O (95:2.5:2.5) for 3 h. Excess TFA was removed by blowing air, and the remaining peptide solution was triturated with cold diethyl ether to precipitate the crude peptide. The precipitated crude peptide and diethyl ether were phase-separated using centrifugation (5900 rpm for 3 min), and the diethyl ether solution was discarded. To remove as much TFA as possible, the washing step was carried out by adding 25 mL of diethyl ether to the crude peptide, vortexing, and centrifugation. This procedure was repeated three times. All centrifuge tubes were tightly sealed with Parafilm to minimize evaporation of diethyl ether during high-speed centrifugation. After centrifuging, the precipitate was dried under vacuum overnight.

The peptides were purified by preparative RP-HPLC with a Varian polymeric column (PLRP-S, 100 Å, 10 μm, 150 × 25 mm) at 25 °C on a Varian ProStar model 325 preparative HPLC (Agilent Technologies, Santa Clara, CA, USA) equipped with a fraction collector. C12FE peptide was dissolved in 20 mL of 0.1% v/v NH_4OH. A water/acetonitrile gradient of 5–100% was run for 30 min containing 0.1% v/v NH_4OH as eluent at a flow rate of 20 mL/min. The crude PemFE peptide was initially dissolved in 20 mL of 0.1% v/v NH_4OH, then diluted with 20 mL of 0.1% v/v TFA. A water/acetonitrile gradient of 5–50% was run for 30 min containing 0.1% v/v TFA as eluent at a flow rate of 20 mL/min. The absorbance peak was monitored at 220 nm. Peptide identity was confirmed by ESI-MS (LDQ Deca ion-trap mass spectrometer, Thermo Finnigan, San Jose, CA, USA). Collected fractions containing desired products were lyophilized (FreeZone −105 °C 4.5 L freeze-dryer, Labconco, Kansas City, MO, USA) and stored at −30 °C.

ESI mass spectra were acquired using a Finnigan LCQ Deca ion-trap mass spectrometer equipped with an electrospray ionization source (Thermo Finnigan) (Supporting Information

S1.2). Analytical RP-HPLC was performed using a Varian polymeric column (PLRP-S, 100 Å, 10 μm, 150 × 4.6 mm) with a 20 μL injection volume (Supporting Information S1.3).

In Vitro MRI CEST Measurement

In vitro CEST MRI images were acquired on a 9.4 T Bruker Avance system equipped with a 15 mm sawtooth RF coil. A modified RARE sequence (TR = 6.0 s, effective TE = 43.2 ms, RARE factor = 16, slice thickness = 1 mm, FOV = 14 × 14 mm, matrix size = 128 × 64, resolution = 0.11 × 0.22 mm^2, and NA = 2) including a magnetization transfer module (one CW pulse, B_1 = 3.6 μT (150 Hz), 3 s) was used to acquire CEST weighted images from −7 to 7 ppm (step = 0.2 ppm) around the water resonance (0 ppm).[84] The absolute water resonant frequency shift was measured using the water saturation shift reference (WASSR)[85] method modified with Lorentzian analysis. The same parameters as in CEST imaging were used except TR = 1.5 s, t_{sat} = 500 ms, B_1 = 0.5 μT (21.3 Hz), and the saturation frequency was swept from −1 to 1 ppm (step = 0.1 ppm). Data processing was performed using custom-written scripts in MATLAB (Mathworks, Natick, MA, USA). CEST spectra were calculated from the mean of an ROI placed over each sample after B_0 correction of the contrast on a per voxel basis. The CEST signal was quantified using MTR_{asym} at particular offsets of interest (*i.e.*, $\Delta\omega$ = +2.2 ppm) using the definition $MTR_{asym} = (S^{-\Delta\omega} - S^{+\Delta\omega})/S_0$, where $S^{[-\Delta\omega,+\Delta\omega]}$ is the water signal intensity in the presence of a saturation pulse at offsets $\pm\Delta\omega$, and S_0 is the water signal intensity in the absence of saturation pulses.

C12FE, PemFE, and Pem samples were prepared at 10 mM in 1× DPBS solution. A pH series ranging from 6.0 to 8.5 with an increment of 0.5 were studied, and sodium hydroxide or hydrochloric acid solution was used to achieve the expected pH. A 1 M solution of sodium hydroxide was prepared by dissolving solid sodium hydroxide in deionized water, while 11 M hydrochloric acid was diluted with water to 1 M hydrochloric acid. Samples were triplicated at each pH. After pH adjustment, samples were transferred to capillary tubes and then arranged on a sample holder. The exchange rate of exchangeable protons of 10 mM Pem, PemFE, and C12FE at different pH's was measured using the modified QUEST method. In brief, the CEST contrast at 5.2 ppm for each sample was measured with saturation delays of 0.5, 1, 1.5, 2, 3, and 6 s, using a saturation field strength of 4.7 μT (200 Hz) and the repetition time (TR) set to 10 s, using the RARE imaging sequence described previously. The calculated MTR_{asym} values were then fit using numerical solutions to the Bloch equations with exchange rate (k_{ex}). The water T1w and T2w were experimentally determined using a saturation recovery spin–echo method and CPMG multiecho spin–echo sequence, respectively. The fixed model parameters were water solute R1s = 0.71 Hz and solute R2s = 39 Hz.

PemFE and C12FE hydrogels were prepared at a final concentration of 30 mM, dissolved in 1× DPBS solution, and sonicated for 2 min to aid in dissolving the lyphophilized powder form of the respective molecules. Samples were aged overnight, and hydrogel photos were taken by inverting both sample vials.

In Vivo MRI Study

All experiments conducted with mice were performed in accordance with protocols approved by the Johns Hopkins University Institutional Animal Care and Use Committee (IACUC). *In vivo* images were acquired on an 11.7 T Bruker Biospec horizontal bore scanner (Bruker Biosciences, Billerica, MA, USA) equipped with a 23 mm circular polarized MRI transceiver volume coil. The same imaging scheme as described above was used with addition of a fat suppression pulse (3.4 ms hermite pulse, offset = −3.5 ppm). The acquisition parameters were TR = 5.0 s, effective TE = 6 ms, RARE factor = 10, t_{sat} = 3 s, B_1 = 3.6 μT (150 Hz), slice thickness = 1 mm, acquisition matrix size = 128 × 64, FOV = 20 × 20 mm, and NA = 2. Due to the B_0 field inhomogeneity, we increased the saturation offset by ±2 ppm (0.1 ppm steps) with respect to water for B_0 mapping.

Supplementary Material

Refer to Web version on PubMed Central for supplementary material.

Acknowledgments

The authors gratefully acknowledge financial support from the National Science Foundation (DMR 1255281) and the National Institutes of Health (NIH/R21EB015609, NIH/R21CA191740, NIH/R01EB019934, and NIH/R03EB021573). In addition, H. Chen is grateful for the support from Key Medicine Discipline Construction of Guangzhou Municipality (grant number 2013-21).

References

1. Morgan CE, Dombrowski AW, Perez CMR, Bahnson ESM, Tsihlis ND, Jiang WL, Jiang Q, Vercammen JM, Prakash VS, Pritts TA, Stupp SI, Kibbe MR. Tissue-Factor Targeted Peptide Amphiphile Nanofibers as an Injectable Therapy To Control Hemorrhage. ACS Nano. 2016; 10:899–909. [PubMed: 26700464]
2. Moyer TJ, Finbloom JA, Chen F, Toft DJ, Cryns VL, Stupp SI. pH and Amphiphilic Structure Direct Supramolecular Behavior in Biofunctional Assemblies. J Am Chem Soc. 2014; 136:14746–14752. [PubMed: 25310840]
3. Newcomb CJ, Sur S, Lee SS, Yu JM, Zhou Y, Snead ML, Stupp SI. Supramolecular Nanofibers Enhance Growth Factor Signaling by Increasing Lipid Raft Mobility. Nano Lett. 2016; 16:3042–3050. [PubMed: 27070195]
4. Lin BF, Megley KA, Viswanathan N, Krogstad DV, Drews LB, Kade MJ, Qian YC, Tirrell MV. pH-Responsive Branched Peptide Amphiphile Hydrogel Designed for Applications in Regenerative Medicine with Potential as Injectable Tissue Scaffolds. J Mater Chem. 2012; 22:19447–19454.
5. Trent A, Marullo R, Lin B, Black M, Tirrell M. Structural Properties of Soluble Peptide Amphiphile Micelles. Soft Matter. 2011; 7:9572–9582.
6. Yaylaci SU, Sen M, Bulut O, Arslan E, Guler MO, Tekinay AB. Chondrogenic Differentiation of Mesenchymal Stem Cells on Glycosaminoglycan-Mimetic Peptide Nanofibers. ACS Biomater Sci Eng. 2016; 2:871–878.
7. Smith DJ, Brat GA, Medina SH, Tong DD, Huang Y, Grahammer J, Furtmuller GJ, Oh BC, Nagy-Smith KJ, Walczak P, Brandacher G, Schneider JP. A multiphase transitioning peptide hydrogel for suturing ultrasmall vessels. Nat Nanotechnol. 2016; 11:95–102. [PubMed: 26524396]
8. Zhou J, Du XW, Xu B. Regulating the Rate of Molecular Self-Assembly for Targeting Cancer Cells. Angew Chem Int Ed. 2016; 55:5770–5775.
9. Zhou J, Du XW, Yamagata N, Xu B. Enzyme-Instructed Self-Assembly of Small *D*-Peptides as a Multiple-Step Process for Selectively Killing Cancer Cells. J Am Chem Soc. 2016; 138:3813–3823. [PubMed: 26966844]

10. Kumar VA, Shi S, Wang BK, Li IC, Jalan AA, Sarkar B, Wickremasinghe NC, Hartgerink JD. Drug-Triggered and Cross-Linked Self-Assembling Nanofibrous Hydrogels. J Am Chem Soc. 2015; 137:4823–4830. [PubMed: 25831137]
11. Kumar VA, Taylor NL, Shi SY, Wang BK, Jalan AA, Kang MK, Wickremasinghe NC, Hartgerink JD. Highly Angiogenic Peptide Nanofibers. ACS Nano. 2015; 9:860–868. [PubMed: 25584521]
12. Kumar VA, Taylor NL, Shi SY, Wickremasinghe NC, D'Souza RN, Hartgerink JD. Self-Assembling Multidomain Peptides Tailor Biological Responses through Biphasic Release. Biomaterials. 2015; 52:71–78. [PubMed: 25818414]
13. Yan C, Altunbas A, Yucel T, Nagarkar RP, Schneider JP, Pochan DJ. Injectable Solid Hydrogel: Mechanism of Shear-Thinning and Immediate Recovery of Injectable Beta-Hairpin Peptide Hydrogels. Soft Matter. 2010; 6:5143–5156. [PubMed: 21566690]
14. Black M, Trent A, Kostenko Y, Lee JS, Olive C, Tirrell M. Self-Assembled Peptide Amphiphile Micelles Containing a Cytotoxic T-Cell Epitope Promote a Protective Immune Response In Vivo. Adv Mater. 2012; 24:3845–3849. [PubMed: 22550019]
15. Chung EJ, Cheng Y, Morshed R, Nord K, Han Y, Wegscheid ML, Auffinger B, Wainwright DA, Lesniak MS, Tirrell MV. Fibrin-Binding, Peptide Amphiphile Micelles for Targeting Glioblastoma. Biomaterials. 2014; 35:1249–1256. [PubMed: 24211079]
16. Cheetham AG, Zhang PC, Lin YA, Lock LL, Cui HG. Supramolecular Nanostructures Formed by Anticancer Drug Assembly. J Am Chem Soc. 2013; 135:2907–2910. [PubMed: 23379791]
17. Kalafatovic D, Nobis M, Son JY, Anderson KI, Ulijn RV. MMP-9 triggered Self-Assembly of Doxorubicin Nanofiber Depots Halts Tumor Growth. Biomaterials. 2016; 98:192–202. [PubMed: 27192421]
18. Pires RA, Abul-Haija YM, Costa DS, Novoa-Carballal R, Reis RL, Ulijn RV, Pashkuleva I. Controlling Cancer Cell Fate Using Localized Biocatalytic Self-Assembly of an Aromatic Carbohydrate Amphiphile. J Am Chem Soc. 2015; 137:576–579. [PubMed: 25539667]
19. Mumcuoglu D, Ekiz MS, Gunay G, Tekinay T, Tekinay AB, Guler MO. Cellular Internalization of Therapeutic Oligonucleotides by Peptide Amphiphile Nanofibers and Nanospheres. ACS Appl Mater Interfaces. 2016; 8:11280–11287. [PubMed: 27097153]
20. Medina SH, Miller SE, Keim AI, Gorka AP, Schnermann MJ, Schneider JP. An Intrinsically Disordered Peptide Facilitates Non-Endosomal Cell Entry. Angew Chem Int Ed. 2016; 55:3369–3372.
21. Sun JEP, Stewart B, Litan A, Lee SJ, Schneider JP, Langhans SA, Pochan DJ. Sustained Release of Active Chemotherapeutics from Injectable-Solid Beta-Hairpin Peptide Hydrogel. Biomater Sci. 2016; 4:839–848. [PubMed: 26906463]
22. Lock LL, Reyes CD, Zhang PC, Cui HG. Tuning Cellular Uptake of Molecular Probes by Rational Design of Their Assembly into Supramolecular Nanoprobes. J Am Chem Soc. 2016; 138:3533–3540. [PubMed: 26890853]
23. Liu S, Zhang PC, Banerjee SR, Xu JD, Pomper MG, Cui HG. Design and Assembly of Supramolecular Dual-Modality Nanoprobes. Nanoscale. 2015; 7:9462–9466. [PubMed: 25967580]
24. Ghosh A, Haverick M, Stump K, Yang XY, Tweedle MF, Goldberger JE. Fine-Tuning the pH Trigger of Self-Assembly. J Am Chem Soc. 2012; 134:3647–3650. [PubMed: 22309293]
25. Lammers T, Kiessling F, Hennink WE, Storm G. Nanotheranostics and Image-Guided Drug Delivery: Current Concepts and Future Directions. Mol Pharmaceutics. 2010; 7:1899–1912.
26. Chakravarty R, Hong H, Cai WB. Positron Emission Tomography Image-Guided Drug Delivery: Current Status and Future Perspectives. Mol Pharmaceutics. 2014; 11:3777–3797.
27. Seymour LW, Ferry DR, Anderson D, Hesslewood S, Julyan PJ, Poyner R, Doran J, Young AM, Burtles S, Kerr DJ, Clin CRCPI-I. Hepatic Drug Targeting: Phase I Evaluation of Polymer-Bound Doxorubicin. J Clin Oncol. 2002; 20:1668–1676. [PubMed: 11896118]
28. Harrington KJ, Mohammadtaghi S, Uster PS, Glass D, Peters AM, Vile RG, Stewart JSW. Effective Targeting of Solid Tumors in Patients with Locally Advanced Cancers by Radiolabeled Pegylated Liposomes. Clin Cancer Res. 2001; 7:243–254. [PubMed: 11234875]
29. Viglianti BL, Ponce AM, Michelich CR, Yu DH, Abraham SA, Sanders L, Yarmolenko PS, Schroeder T, MacFall JR, Barboriak DP, Colvin OM, Bally MB, Dewhirst MW. Chemodosimetry

of *In Vivo* Tumor Liposomal Drug Concentration Using MRI. Magn Reson Med. 2006; 56:1011–1018. [PubMed: 17029236]

30. Langereis S, Geelen T, Grull H, Strijkers GJ, Nicolay K. Paramagnetic Liposomes for Molecular MRI and MRI-Guided Drug Delivery. NMR Biomed. 2013; 26:728–744. [PubMed: 23703874]
31. Bohmer MR, Klibanov AL, Tiemann K, Hall CS, Gruell H, Steinbach OC. Ultrasound Triggered Image-Guided Drug Delivery. Eur J Radiol. 2009; 70:242–253. [PubMed: 19272727]
32. Su Z, Shen H, Wang H, Wang J, Li J, Nienhaus GU, Shang L, Wei G. Motif-Designed Peptide Nanofibers Decorated with Graphene Quantum Dots for Simultaneous Targeting and Imaging of Tumor Cells. Adv Funct Mater. 2015; 25:5472–5478.
33. Yang Z, Lee JH, Jeon HM, Han JH, Park N, He Y, Lee H, Hong KS, Kang C, Kim JS. Folate-Based Near-Infrared Fluorescent Theranostic Gemcitabine Delivery. J Am Chem Soc. 2013; 135:11657–62. [PubMed: 23865715]
34. Wu X, Sun X, Guo Z, Tang J, Shen Y, James TD, Tian H, Zhu W. *In Vivo* and *In Situ* Tracking Cancer Chemotherapy by Highly Photostable NIR Fluorescent Theranostic Prodrug. J Am Chem Soc. 2014; 136:3579–88. [PubMed: 24524232]
35. Lock LL, Cheetham AG, Zhang PC, Cui HG. Design and Construction of Supramolecular Nanobeacons for Enzyme Detection. ACS Nano. 2013; 7:4924–4932. [PubMed: 23682734]
36. Mao XP, Xu JD, Cui HG. Functional Nanoparticles for Magnetic Resonance Imaging. WIREs Nanomed Nanobiotechnol. 2016; 8:814–841.
37. Bull SR, Guler MO, Bras RE, Meade TJ, Stupp SI. Self-Assembled Peptide Amphiphile Nanofibers Conjugated to MRI Contrast Agents. Nano Lett. 2005; 5:1–4. [PubMed: 15792402]
38. Bull SR, Guler MO, Bras RE, Venkatasubramanian PN, Stupp SI, Meade TJ. Magnetic Resonance Imaging of Self-Assembled Biomaterial Scaffolds. Bioconjugate Chem. 2005; 16:1343–1348.
39. Preslar AT, Parigi G, McClendon MT, Sefick SS, Moyer TJ, Haney CR, Waters EA, MacRenaris KW, Luchinat C, Stupp SI, Meade TJ. Gd(III)-Labeled Peptide Nanofibers for Reporting on Biomaterial Localization *In Vivo*. ACS Nano. 2014; 8:7325–7332. [PubMed: 24937195]
40. Ghosh A, Buettner CJ, Manos AA, Wallace AJ, Tweedle MF, Goldberger JE. Probing Peptide Amphiphile Self-Assembly in Blood Serum. Biomacromolecules. 2014; 15:4488–4494. [PubMed: 25347387]
41. Grobner T. Gadolinium–A Specific Trigger for the Development of Nephrogenic Fibrosing Dermopathy and Nephrogenic Systemic Fibrosis? Nephrol Dial Transplant. 2006; 21:1104–1108. [PubMed: 16431890]
42. Kanda T, Fukusato T, Matsuda M, Toyoda K, Oba H, Kotoku JI, Haruyama T, Kitajima K, Furui S. Gadolinium-Based Contrast Agent Accumulates in the Brain Even in Subjects Without Severe Renal Dysfunction: Evaluation of Autopsy Brain Specimens with Inductively Coupled Plasma Mass Spectroscopy. Radiology. 2015; 276:142690.
43. Ward KM, Aletras AH, Balaban RS. A New Class of Contrast Agents for MRI Based on Proton Chemical Exchange Dependent Saturation Transfer (CEST). J Magn Reson. 2000; 143:79–87. [PubMed: 10698648]
44. Liu GS, Song XL, Chan KWY, McMahon MT. Nuts and Bolts of Chemical Exchange Saturation Transfer MRI. NMR Biomed. 2013; 26:810–828. [PubMed: 23303716]
45. Liu GS, Liang YJ, Bar-Shir A, Chan KWY, Galpoththawela CS, Bernard SM, Tse T, Yadav NN, Walczak P, McMahon MT, Bulte JWM, van Zijl PCM, Gilad AA. Monitoring Enzyme Activity Using a Diamagnetic Chemical Exchange Saturation Transfer Magnetic Resonance Imaging Contrast Agent. J Am Chem Soc. 2011; 133:16326–16329. [PubMed: 21919523]
46. McVicar N, Li AX, Goncalves DF, Bellyou M, Meakin SO, Prado MAM, Bartha R. Quantitative Tissue pH Measurement During Cerebral Ischemia Using Amine and Amide Concentration-Independent Detection (AACID) with MRI. J Cereb Blood Flow Metab. 2014; 34:690–698. [PubMed: 24496171]
47. Zhou JY, Payen JF, Wilson DA, Traystman RJ, van Zijl PCM. Using the Amide Proton Signals of Intracellular Proteins and Peptides to Detect pH Effects in MRI. Nat Med. 2003; 9:1085–1090. [PubMed: 12872167]

48. Yang X, Song XL, Li YG, Liu GS, Banerjee SR, Pomper MG, McMahon MT. Salicylic Acid and Analogues as diaCEST MRI Contrast Agents with Highly Shifted Exchangeable Proton Frequencies. Angew Chem Int Ed. 2013; 52:8116–8119.
49. Longo DL, Dastru W, Digilio G, Keupp J, Langereis S, Lanzardo S, Prestigio S, Steinbach O, Terreno E, Uggeri F, Aime S. Iopamidol as a Responsive MRI-Chemical Exchange Saturation Transfer Contrast Agent for pH Mapping of Kidneys: *In Vivo* Studies in Mice at 7 T. Magn Reson Med. 2011; 65:202–211. [PubMed: 20949634]
50. Chen LQ, Howison CM, Jeffery JJ, Robey IF, Kuo PH, Pagel MD. Evaluations of Extracellular pH within *In Vivo* Tumors Using acidoCEST MRI. Magn Reson Med. 2014; 72:1408–1417. [PubMed: 24281951]
51. Chen LQ, Randtke EA, Jones KM, Moon BF, Howison CM, Pagel MD. Evaluations of Tumor Acidosis within *In Vivo* Tumor Models Using Parametric Maps Generated with AcidoCEST MRI. Mol Imaging Biol. 2015; 17:488–496. [PubMed: 25622809]
52. Longo DL, Sun PZ, Consolino L, Michelotti FC, Uggeri F, Aime S. A General MRI-CEST Ratiometric Approach for pH Imaging: Demonstration of *In Vivo* pH Mapping with Lobitridol. J Am Chem Soc. 2014; 136:14333–14336. [PubMed: 25238643]
53. Li Y, Chen H, Xu J, Yadav NN, Chan KWY, Luo L, McMahon MT, Vogelstein B, van Zijl PCM, Zhou S, Liu G. CEST Theranostics: Label-Free MR Imaging of Anticancer Drugs. Oncotarget. 2016; 7(6):6369–6378. [PubMed: 26837220]
54. Liu H, Jablonska A, Li Y, Cao S, Liu D, Chen H, Van Zijl PC, Bulte JW, Janowski M, Walczak P, Liu G. Label-free CEST MRI Detection of Citicoline-Liposome Drug Delivery in Ischemic Stroke. Theranostics. 2016; 6:1588–600. [PubMed: 27446492]
55. Snoussi K, Bulte JW, Guéron M, van Zijl P. Sensitive CEST Agents Based On Nucleic Acid Imino Proton Exchange: Detection of Poly (rU) and of a Dendrimer-Poly (rU) Model for Nucleic Acid Delivery and Pharmacology. Magn Reson Med. 2003; 49:998–1005. [PubMed: 12768576]
56. Choi J, Kim K, Kim T, Liu G, Bar-Shir A, Hyeon T, McMahon MT, Bulte JW, Fisher JP, Gilad AA. Multimodal Imaging of Sustained Drug Release from 3-D Poly (propylene fumarate) (PPF) Scaffolds. J Controlled Release. 2011; 156:239–245.
57. Song X, Airan RD, Arifin DR, Bar-Shir A, Kadayakkara DK, Liu G, Gilad AA, van Zijl PC, McMahon MT, Bulte JW. Label-free *In Vivo* Molecular Imaging of Underglycosylated Mucin-1 Expression in Tumour Cells. Nat Commun. 2015; 6:6719. [PubMed: 25813863]
58. Dula AN, Arlinghaus LR, Dortch RD, Dewey BE, Whisenant JG, Ayers GD, Yankeelov TE, Smith SA. Amide Proton Transfer Imaging of the Breast at 3 T: Establishing Reproducibility and Possible Feasibility Assessing Chemotherapy Response. Magn Reson Med. 2013; 70:216–224. [PubMed: 22907893]
59. Sagiyama K, Mashimo T, Togao O, Vemireddy V, Hatanpaa KJ, Maher EA, Mickey BE, Pan E, Sherry AD, Bachoo RM. *In Vivo* Chemical Exchange Saturation Transfer Imaging Allows Early Detection of a Therapeutic Response in Glioblastoma. Proc Natl Acad Sci USA. 2014; 111:4542–4547. [PubMed: 24616497]
60. Zhao F, Ma ML, Xu B. Molecular Hydrogels of Therapeutic Agents. Chem Soc Rev. 2009; 38:883–891. [PubMed: 19421568]
61. Lin R, Cheetham AG, Zhang PC, Lin YA, Cui HG. Supramolecular Filaments Containing a Fixed 41% Paclitaxel Loading. Chem Commun. 2013; 49:4968–4970.
62. Lin YA, Cheetham AG, Zhang PC, Ou YC, Li YG, Liu GS, Hermida-Merino D, Hamley IW, Cui HG. Multiwalled Nanotubes Formed by Catanionic Mixtures of Drug Amphiphiles. ACS Nano. 2014; 8:12690–12700. [PubMed: 25415538]
63. Lock LL, LaComb M, Schwarz K, Cheetham AG, Lin YA, Zhang P, Cui H. Self-Assembly of Natural and Synthetic Drug Amphiphiles into Discrete Supramolecular Nanostructures. Faraday Discuss. 2013; 166:285–301. [PubMed: 24611283]
64. Ma W, Cheetham AG, Cui HG. Building Nanostructures with Drugs. Nano Today. 2016; 11:13–30. [PubMed: 27066106]
65. Su H, Koo JM, Cui HG. One-Component Nanomedicine. J Controlled Release. 2015; 219:383–395.

66. Su H, Zhang PC, Cheetham AG, Koo JM, Lin R, Masood A, Schiapparelli P, Quinones-Hinojosa A, Cui HG. Supramolecular Crafting of Self-Assembling Camptothecin Prodrugs with Enhanced Efficacy against Primary Cancer Cells. Theranostics. 2016; 6:1065–1074. [PubMed: 27217839]

67. Hazarika M, White RM, Johnson JR, Pazdur R. FDA Drug Approval Summaries: Pemetrexed (Alimta (R)). Oncologist. 2004; 9:482–488. [PubMed: 15477632]

68. Nel AE, Madler L, Velegol D, Xia T, Hoek EMV, Somasundaran P, Klaessig F, Castranova V, Thompson M. Understanding Biophysicochemical Interactions at the Nano-Bio Interface. Nat Mater. 2009; 8:543–557. [PubMed: 19525947]

69. Gazit E. A Possible Role for Pi-Stacking in the Self-Assembly of Amyloid Fibrils. FASEB J. 2002; 16:77–83. [PubMed: 11772939]

70. Guo C, Luo Y, Zhou RH, Wei GH. Probing the Self-Assembly Mechanism of Diphenylalanine-Based Peptide Nanovesicles and Nanotubes. ACS Nano. 2012; 6:3907–3918. [PubMed: 22468743]

71. Ma ML, Kuang Y, Gao Y, Zhang Y, Gao P, Xu B. Aromatic-Aromatic Interactions Induce the Self-Assembly of Pentapeptidic Derivatives in Water to Form Nanofibers and Supramolecular Hydrogels. J Am Chem Soc. 2010; 132:2719–2728. [PubMed: 20131781]

72. Fleming S, Ulijn RV. Design of Nanostructures Based on Aromatic Peptide Amphiphiles. Chem Soc Rev. 2014; 43:8150–8177. [PubMed: 25199102]

73. Bakota EL, Sensoy O, Ozgur B, Sayar M, Hartgerink JD. Self-Assembling Multidomain Peptide Fibers with Aromatic Cores. Biomacromolecules. 2013; 14:1370–1378. [PubMed: 23480446]

74. Hamley IW, Dehsorkhi A, Castelletto V, Furzeland S, Atkins D, Seitsonen J, Ruokolainen J. Reversible Helical Unwinding Transition of a Self-Assembling Peptide Amphiphile. Soft Matter. 2013; 9:9290–9293.

75. Duncan R. Polymer Conjugates as Anticancer Nanomedicines. Nat Rev Cancer. 2006; 6:688–701. [PubMed: 16900224]

76. Cui HG, Cheetham AG, Pashuck ET, Stupp SI. Amino Acid Sequence in Constitutionally Isomeric Tetrapeptide Amphiphiles Dictates Architecture of One-Dimensional Nanostructures. J Am Chem Soc. 2014; 136:12461–12468. [PubMed: 25144245]

77. Yu ZL, Tantakitti F, Yu T, Palmer LC, Schatz GC, Stupp SI. Simultaneous Covalent and Noncovalent Hybrid Polymerizations. Science. 2016; 351:497–502. [PubMed: 26823427]

78. Cui H, Webber MJ, Stupp SI. Self-Assembly of Peptide Amphiphiles: From Molecules to Nanostructures To Biomaterials. Biopolymers. 2010; 94:1–18. [PubMed: 20091874]

79. Liu G, Moake M, Har-el YE, Long CM, Chan KW, Cardona A, Jamil M, Walczak P, Gilad AA, Sgouros G, van Zijl PC, Bulte JW, McMahon MT. *In Vivo* Multicolor Molecular MR Imaging Using Diamagnetic Chemical Exchange Saturation Transfer Liposomes. Magn Reson Med. 2012; 67:1106–13. [PubMed: 22392814]

80. Michalak O, Gruza MM, Witkowska A, Bujak I, Cmoch P. Synthesis and Physicochemical Characterization of the Impurities of Pemetrexed Disodium, an Anticancer Drug. Molecules. 2015; 20:10004–10031. [PubMed: 26035100]

81. Liepinsh E, Otting G. Proton Exchange Rates from Amino Acid Side Chains - Implications For Image Contrast. Magn Reson Med. 1996; 35:30–42. [PubMed: 8771020]

82. Berndt KD, Beunink J, Schroder W, Wuthrich K. Designed Replacement of an Internal Hydration Water Molecule in Bpti -Structural and Functional Implications of a Glycine-to-Serine Mutation. Biochemistry. 1993; 32:4564–4570. [PubMed: 7683491]

83. McMahon MT, Gilad AA, Zhou JY, Sun PZ, Bulte JWM, van Zijl PCM. Quantifying Exchange Rates in Chemical Exchange Saturation Transfer Agents Using the Saturation Time and Saturation Power Dependencies of the Magnetization Transfer Effect on the Magnetic Resonance Imaging Signal (QUEST and QUESP): pH Calibration for Poly-L-Lysine and a Starburst Dendrimer. Magn Reson Med. 2006; 55:836–847. [PubMed: 16506187]

84. Liu G, Gilad AA, Bulte JW, van Zijl PC, McMahon MT. High-Throughput Screening of Chemical Exchange Saturation Transfer MR Contrast Agents. Contrast Media Mol Imaging. 2010; 5:162–70. [PubMed: 20586030]

85. Kim M, Gillen J, Landman BA, Zhou J, Zijl PCMV. Water Saturation Shift Referencing (WASSR) for Chemical Exchange Saturation Transfer (CEST) experiments. Magn Reson Med. 2009; 61:1441–1450. [PubMed: 19358232]

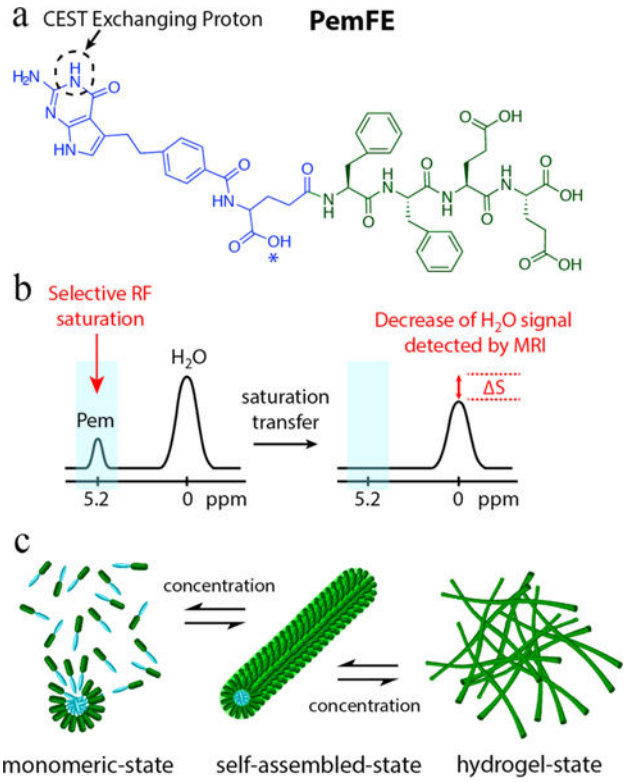

Figure 1.

(a) Chemical structure of the studied PemFE molecule with the CEST MRI signal originating from the aromatic amine exchangeable proton on Pem (blue). A possible PemFE structural isomer conjugation site is indicated by an asterisk (*). (b) CEST contrast is measured by a decrease in water signal when the selectively saturated 5.2 ppm exchangeable proton is within supramolecular filaments and hydrogels. (c) Schematic illustration of the self-assembly of PemFE monomers into filamentous nanostructures that can further entangle into a 3D network for formation of self-supporting hydrogels under suitable conditions (pH, concentration, and ionic strength).

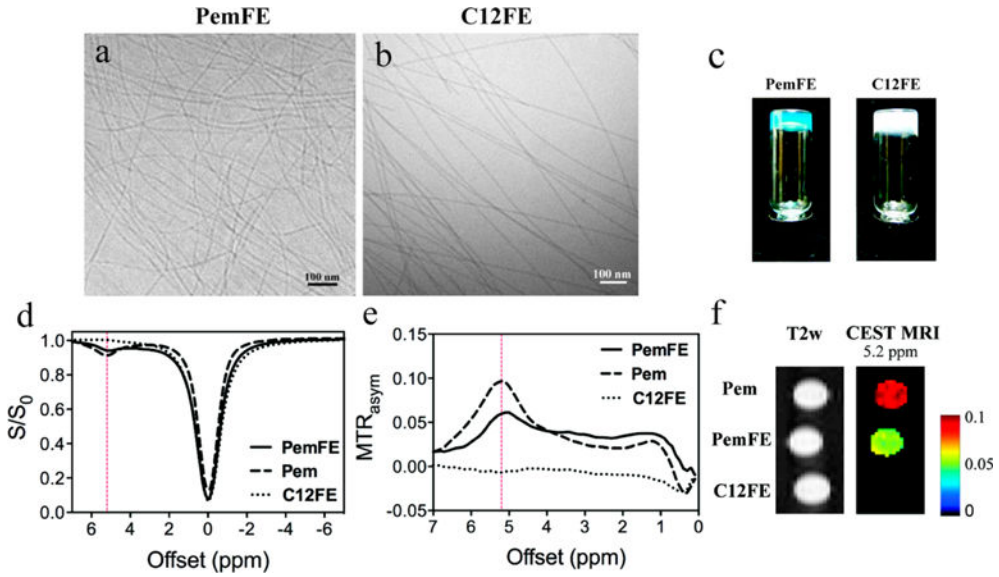

Figure 2.

Cryo-TEM micrographs of (a) PemFE, 4 mM, and (b) C12FE control molecule, 10 mM, revealing filamentous nanostructures of 9.1 ± 1.4 and 8.5 ± 0.9 nm diameter, respectively. (c) Digital photographs of PemFE and C12FE in a 30 mM 1× DPBS solution after overnight ageing, demonstrating formation of self-supporting hydrogels. (d–f) CEST properties of 10 mM Pem, PemFE, and C12FE at pH 7.4 and 37 °C, with (d) CEST spectra and (e) MTR_{asym} plots of PemFE (solid), Pem (dashed), and C12FE (dotted) showing CEST peaks at 5.2 ppm. (f) Color-coded CEST contrast map of Pem, PemFE, and C12FE with respect to the 5.2 ppm offset from water.

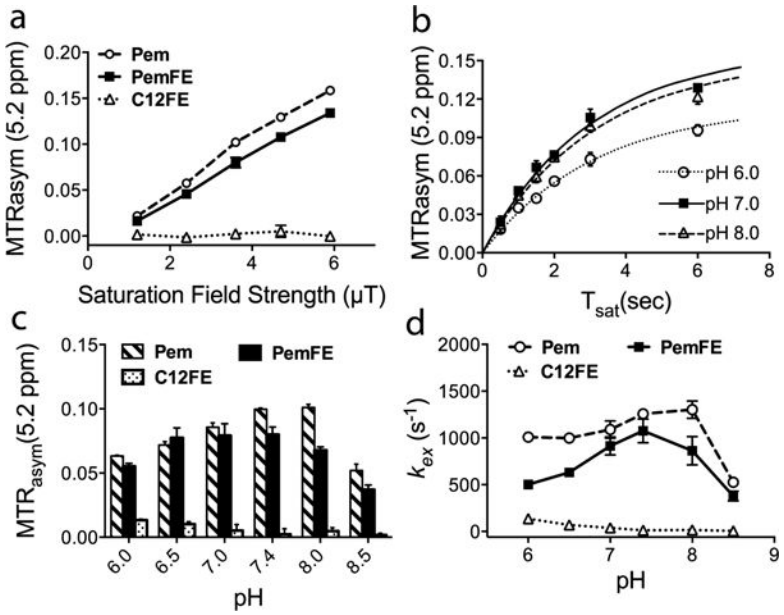

Figure 3.

CEST properties of PemFE, Pem, and C12FE, each in a 10 mM 1× DPBS solution at 37 °C. (a) MTR_{asym} at 5.2 ppm of all designed molecules at pH 7.4, measured at different saturation field strength. (b) PemFE MTR_{asym} at 5.2 ppm measured with respect to presaturation time (T_{sat}) at pH 6, 7, and 8. (c) MTR_{asym} at 5.2 ppm as a function of pH using $B_1 = 3.6\ \mu T$. A quantifying exchange using the saturation time (QUEST) method was used to fit data and obtain k_{ex} values. (d) pH dependence of proton exchange rate (k_{ex}) as a function of pH using $B_1 = 3.6\ \mu T$.

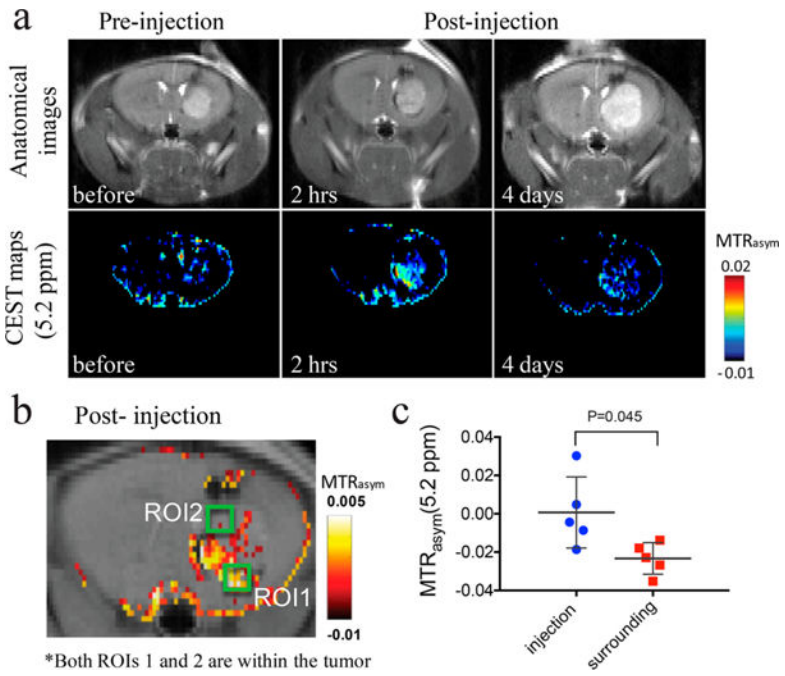

Figure 4.

MRI detection of a PemFE nanofiber hydrogel that was stereotactically injected in mouse brain tumors (day 25 after tumor implantation). (a) On the top, MRI images showing GL261 brain tumor at different time points (with respect to the time of injection of the nanofiber hydrogel); on the bottom, CEST maps at 5.2 ppm of the mouse brain before, and 2 h and 4 days after PemFE injection. (b) Illustration of chosen ROIs on overlaid CEST images at 2 h after the PemFE hydrogel injection to represent tumor regions of ROI1 (the PemFE injection site with increased CEST contrast) and ROI2 (its surrounding region, without CEST contrast). (c) Quantification of CEST contrast showing a significantly higher MTR_{asym} value for the PemFE injection site than surrounding tumor ($P > 0.05$, two-tailed, paired Student's *t*-test, $n = 5$).